NIPER-582
(DE92001047)

IMAGING TECHNIQUES APPLIED TO THE STUDY OF FLUIDS IN POROUS MEDIA

By
L. Tomutsa
D. Doughty
A. Brinkmeyer
S. Mahmood

June 1992

Performed Under Cooperative Agreement No. FC22-83FE60149

IIT Research Institute
National Institute for Petroleum and Energy Research
Bartlesville, Oklahoma

Bartlesville Project Office
U. S. DEPARTMENT OF ENERGY
Bartlesville, Oklahoma

NIPER-582
Distribution Category UC-122

NIPER--582

DE92 001047

IMAGING TECHNIQUES APPLIED TO THE STUDY OF FLUIDS IN POROUS MEDIA

By
L. Tomutsa
D. Doughty
A. Brinkmeyer
S. Mahmood

June 1992

Work Performed Under Cooperative Agreement No. FC22-83FE60149

Prepared for
U.S. Department of Energy
Assistant Secretary for Fossil Energy

R. L. Lemmon, Project Manager
Bartlesville Project Office
P. O. Box 1398
Bartlesville, OK 74005

Prepared by
IIT Research Institute
National Institute for Petroleum and Energy Research
P. O. Box 2128
Bartlesville, OK 74005

TABLE OF CONTENTS

TABLES

ILLUSTRATIONS

IMAGING TECHNIQUES APPLIED TO THE STUDY OF FLUIDS IN POROUS MEDIA

By L. Tomutsa, D. Doughty, A. Brinkmeyer, and S. Mahmood

ABSTRACT

Improved imaging techniques were used to study the dynamics of fluid flow and trapping at various scales in porous media. Two-phase and three-phase floods were performed and monitored by computed tomography (CT) scanning and/or nuclear magnetic resonance imaging (NMRI) microscopy. Permeability-porosity correlations obtained from image analysis were combined with porosity distributions from CT scanning to generate spatial permeability distributions within the core which were used in simulations of two-phase floods. Simulation-derived saturation distributions of two-phase processes showed very good agreement with the CT measured values. To increase the efficiency, the accuracy, and the versatility of the CT scanning facility, a computer controlled, high accuracy (±12 microns) positioning table and an image processing workstation were installed. By directly interfacing the CT scanner to the workstation for three-dimensional (3-D) image analysis, the image processing speed and the computational capabilities needed to calculate porosity and multiphase fluid saturations were considerably increased. Improved gas saturations were measured by CT scanning and progress was made toward accurate measurement of three-phase saturations. Newly constructed gradient coils and probe and improved data acquisition and processing yielded the highest spatial resolution (20 microns) of fluid in porous media to date by use of NMRI microscopy. This capability, which allows clear 3-D displays of the oil and water phases within a pore system, was used to identify the effect of pore structure on residual oil and water saturations. The improvements in the imaging capabilities allowed the expansion of the use of the imaging facility to support other base programs and projects for industrial clients. A videotape, which highlights the potential applications of the thin slab micromodel technology for the pore level study of fluids, has been produced, as an instrument for technology transfer.

INTRODUCTION

This project is aimed at advancing the understanding of fundamental processes involved in oil recovery by developing, applying, and refining cross-cutting imaging techniques and technologies. The techniques developed in this project are being used to characterize pore structures and surfaces, pore-to-core scale heterogeneities, rock-fluid interactions, and distribution of fluids in reservoir rock during corefloods. This project supports reservoir description and advanced oil recovery processes research and development, especially in the areas of reservoir chemistry, physics, and rock-fluid interactions at the micro- and macroscopic scales (pore to whole core scales). Techniques developed in this project have been applied to understanding the rock fabric of various facies, the effect of various polymer/surfactant combinations on oil recovery, to characterize and select the most representative core plugs for special core analyses, to understand the effect of fractures on EOR processes designed for industrial clients, to characterize formation heterogeneities for an improved understanding of log response to them, and to identify the effect of saturation distributions on the electrical resistivity of core samples.[1] A longer-term goal is the application of techniques developed in this project to the study of oil trapping, recovery mechanisms, and scaling-up procedures from core plug to whole core to interwell scales, and to developing novel enhanced oil recovery processes. Other applications include estimates of water and gas content in coal samples from coal bed methane producing formations.

This work addresses the goal of developing and testing technologies designed to overcome specific problems that prevent increased oil recovery that is part of the National Energy Strategy.[2] In addition the goal of the transfer of federally developed technology to the petroleum industry is accomplished in this project through the application of imaging technology to "real-world" problems in industrial funded projects.

In response to increased demand by several other projects for use of the CT scanning facility and of NMRI microscopy in observing multiphase fluid distributions in reservoir rock at scales ranging from microns to inches, technical improvements have been implemented in the rock-fluid imaging laboratory. Progress has been made in integrating the various rock-fluid imaging techniques to quantify the effect of rock heterogeneities on oil recovery.

The computer aided image analysis system for automatic measurements of pores, pore throats, and grain sizes from thin sections of reservoir rock has been used to generate grain size distributions for facies classification for reservoir characterization and small-scale permeability-porosity correlations for permeability calculations within cores. These correlations were used together with porosity distributions from CT scans to generate permeability distributions in a rock sample for which porosity distributions were generated by CT scanning. The permeability spatial distributions generated were used as part of the input in simulating two-phase fluid flow in a rock sample.

CT technology is a powerful tool for nondestructive measurement of variations in rock properties and fluid saturations in reservoir rock. NIPER acquired a third-generation CT scanner in 1989, which, together with software developed at NIPER for image processing and analysis, was used in FY90 to study the ability to provide

quantitative time-dependent measurements of oil, brine, and gas spatial saturation distributions in cores during flow experiments. Recently implemented rapid data transfer from the CT to an image processing workstation allows real time image transfer. Large numbers of scans can be performed and processed by state-of-the-art 3-D image processing software, thus taking full advantage of the rapid scan time (20 sec/scan) of the CT scanner. Studies of flow processes are currently performed at ambient conditions; however, operators are interested in recovery processes at reservoir pressure and temperature conditions. A coreholder designed for whole core experiments at temperatures up to 300° F and pressures of 10,000 psi will be available soon. A positioning table with 5 ft of total travel distance and accuracy better than 20 microns has been installed. This not only improves the accuracy of porosity and saturation calculations, which require multiple scans at precisely the same locations, but also increases the instrument efficiency by allowing multiple experiments to be run on the CT scanner. Core floods can be performed and monitored by CT on more than one core simultaneously, because cores can be moved in and out of the the CT gantry and repositioned accurately for CT imaging. Also, while a coreflood is performed on one core, another core can be scanned for rapid determination of core heterogeneites and for selection of representative core plug samples from whole core for special core analysis.

Nuclear magnetic resonance imaging is another nondestructive imaging technology used to image fluids within core. NIPER is working on NMRI developments in (a) spatial resolution, (b) image processing techniques, and (c) resolution of oil and water phases. A commercial high-resolution Fourier Transform NMR spectrometer has been modified to be used as an imaging instrument. The NIPER NMR instrument has already been used to generate 3-D images of fluids in cores with resolutions as low as 25 microns. A maximum image resolution of 10 microns is anticipated, based on the high field, the small bore of the spectrometer's superconducting magnet, and other instrument characteristics. By comparison, commercial NMRI instruments used for medical or core imaging purposes generally have resolutions in the 300 to 500 micron range. The high resolution achievable allows visualization of the effect of rock/fluid interaction on oil, water, and gas distributions within pore spaces of reservoir rocks. Such a capability aids in understanding oil displacement processes taking place at the pore level and is essential in understanding the mechanisms of various oil recovery processes. Previous image acquisition and processing speed limitations have been improved by interfacing two high speed personal computers with the NMR spectrometer. The image data acquisition system uses recently constructed high magnetic field gradient coils and a probe of improved design. A 25 MHz 386 PC controls the current in the high magnetic field gradient coils and acquires the image data. The image data then are transferred to a dedicated, 33 MHz 386 PC for processing. Pore level fluid displacement using micromodels is a new technique that has been developed at NIPER using thin-slab (3-mm) micromodels built from sandstone samples. Pore-level fluid flow and fluid displacement processes for oil, gas, and water phases have been observed by optical microscopy. This technique, combined with flow experiments performed on cores, is used to improve the understanding of mechanisms by which various oil recovery processes remove oil from reservoir rock. This technique can help in the design of an optimum recovery process for a given reservoir rock by enabling observations, at the pore level, of the effects of various flow regimes, fluid properties, and injected chemicals on oil mobilization. Work this year was focussed on processing images generated in experiments in previous years and creating a videotape which highlights the potential applications of this technology for the pore level study of fluids.

CT IMAGING

Equipment Modifications

The adaptation of a medical computed tomography (CT) scanner for use in studies of core heterogeneities and fluid distributions within core samples required equipment hardware/software modifications and additions. This fiscal year the modifications were primarily concentrated on (1) interfacing the CT scanner's host computer, a PDP 11/34, with a Macintosh IIfx based image processing/analysis workstation; (2) installation of a high accuracy positioning system; and (3) installation of a 3-D image analysis and processing system on the Macintosh workstation.

A system based on the 40 MHz Macintosh IIfx, 210 MB hard drive, 20 MB RAM, and a 19-in. color monitor was acquired. Conversion programs for the data files were written, and both 2-D and 3-D reconstructions of CT and NMR images have been displayed. The interfacing of the PDP 11/34 to the Macintosh IIfx enabled the rapid transfer of CT generated images to image processing software for quantitative and qualitative analysis. Previous interfacing capabilities were through the RS 232C ports of each machine requiring approximately 8 to 10 minutes to download a single CT image (130 Kb of data). This was a considerable handicap when considering the large amounts of data needed to image a small-scale coreflood or to characterize a section of core. The new interface, with associated software, permits either the capturing of CT images to the workstation in real time or downloading after completion of a scan. Total transfer time of a single CT image is now less than 10 seconds. The hardware interface between the PDP's Unibus and the Macintosh's Nubus was accomplished through the use of a general purpose interface that is currently in the PDP (the DR11-C), a 32 bit digital input/output board that was installed on the Macintosh bus (NB-DIO-32F), and a board, built at NIPER, that acts as a data buffer and a data ready line signal flip-flop between the DR11-C and the NB-DIO-32F. The DR11-C provides the logic and memory buffers necessary for the program-controlled parallel transfer of 16 bit data from the PDP. The go-between board essentially acts as a storage device for the 16 bit data and a duration extender for the data ready line used in the handshake between the two interfaces. The

NB-DIO-32F receives the incoming data and makes it available on the Macintosh workstation. In-house software was written to coordinate the parallel transfer of the 16 bit images between the two machines. A schematic diagram of the CT scanning system and the interface is shown in Fig. 1.

To calculate porosity and saturation distributions in a core accurately, a number of scans at various saturation conditions have to be performed at precisely the same location of the sample. A new positioning system with a repeatability of ±12 microns was designed to satisfy this requirement. The previous positioning repeatability was approximately ±2 mm. This was inadequate since the alignment of the rock for porosity and saturation calculations required repositioning with a repeatability of at least ±0.1 mm. The new system consists of a stepping motor with a programmable indexer/driver and an absolute encoder for position reference, position maintenance, and position repeatability. The system is remotely controlled from one of three sources: the Macintosh workstation, a PC based system, or a dedicated laptop computer that can be placed next to the CT scanner to facilitate the initial positioning of the sample in the X-ray beam. In addition to the high resolution position repeatability, the new CT scanning system provides bidirectional software and hardware limit switches for end-of-travel protection, and programmable control of an infinite number of absolute moves allowing for minimal operator assistance. Figure 2 shows a schematic diagram of the CT positioning system.

Recently, a data display and analysis software package developed at the National Center for Supercomputer Applications (NCSA), University of Illinois, modified for use on Apple Mac II computers, has been made available under the trademark of SPYGLASS. This software package allows viewing of any 3-D object sections along planes parallel to XY, XZ, and YZ planes as well as rotation of the 3-D object around the X, Y, and Z axes. Various color tables as well as a gray scale are available for the data display. By stacking up 2-D sections and using the transparency mode, which associates background color to selected data value ranges, one can display 3-D distributions of physical properties with values only within the range of interest. Porosity, permeability, or saturations from CT applications or water and oil distributions at pore level from high resolution NMRI applications can be readily displayed. This software package also has the advantage of compatibility with the NIPER network which uses Macintosh computers for reports and presentations. The initial experimental work concentrated on testing the compatibility and capabilities of the different components of the CT imaging system. The first test involved scanning an epoxy encapsulated rectangular Shannon slab in planes parallel to the largest cross section at 2-mm intervals. The CT image files were downloaded to the image workstation, and a three-dimensional image of the CT density distribution was generated. Figure 3 shows the density distribution of the Shannon slab with a portion of the slab "cut out" to facilitate viewing of the CT densities in the middle regions of the rock. The darker areas are lower CT densities representative of higher porosity regions, whereas the lighter areas are indicative of more dense or lower porosity regions. Similarly, a cylindrical heterogeneous Berea sample, contained in a magnesium alloy coreholder, was scanned at 53 adjacent positions perpendicular to the axis of the core. Figure 4 shows the 3-D image of the CT density distribution in the Berea sandstone.

By automating the image acquisition and the table positioning, and by providing a means of image processing and analyses, the capabilities of conducting accurate, time-efficient coreflood research projects in conjunction with industrial client core screening projects have been significantly enhanced.

Experimental

Two-phase corefloods

The method to determine the porosity distribution within porous media using CT scanning has been described.[3] This work was expanded to integrate the information generated from the petrographical image analysis system (PIA)[4] with the spatial distribution data obtained from the CT to attain a reliable method of predicting permeability distribution within the core. Figure 5 shows the permeability-porosity correlation for the Shannon slab studied derived from PIA of images from a representative thin section. Figure 6 shows the porosity and permeability distributions for the Shannon slab generated from a 2-mm CT slice using the correlation shown in Fig. 5.

Coreflood simulations were performed to test the validity of this method of calculating core permeability distributions by integrating PIA data with CT data. Data input for the porosity and permeability grids needed by the BOAST-VHS simulator were values obtained from the CT porosity and permeability distributions of the Shannon slab. The agreement between the fluid saturations calculated by the simulator shown in Fig. 7 and by the CT shown in Fig. 8, with strong fingering in the high permeability layer, indicates the potential for this permeability determination method for samples in which a good permeability-porosity correlation can be generated by PIA.

Work continued toward improving the accuracy of gas saturation measurements with the CT scanner. Gas flood experiments on a 3-in.-long by 1.5-in.-diameter brine saturated Bentheimer sandstone core were conducted to test the resolution of the CT scanner in gas detection. CT slices of 8-mm thickness were taken perpendicular to the longitudinal axis of the core at seven different saturation stages of the gas flood, numbered 1 to 7 in Figs. 9 and 10. The average gas saturations for the various cross-section locations along the core, calculated from CT, are shown in Fig. 9. Average gas saturations for the entire core, calculated from the CT scanner and volumetrically, for the seven saturation stages are shown in Fig. 10. From Fig. 10 it can be seen that as the gas flood proceeded above 40% gas saturation, the difference between the volumetric and the CT saturation values increased systematically. At gas

saturations below 40%, the agreement between the two values was excellent (less than 1% deviation), and at gas saturations of 70% the discrepancy became 6%. Further work is needed to improve the reliability of measurements at high gas saturations.

Three-phase corefloods

To measure the recovery efficiency in immiscible CO_2 floods and water-alternate-gas (WAG) recovery processes, accurate determinations of three-phase saturation distributions in the reservoir rock are needed. Methods were explored for measuring three-phase (gas, oil, and brine) saturations using the CT scanner. While for porosity and two-phase saturation measurements, CT scanning at one X-ray energy is adequate, for three-phase fluid saturation measurements in a porous media, it is necessary that the media be scanned at two different X-ray energy levels . The equations for calculating porosity and saturation using single energy are given below:[3]

Porosity

$$\phi = (Y_{bm}-Y_{gm})/(Y_{brine}-Y_{gas}) \quad (1)$$

where:

ϕ = Porosity
Y_{bm} = CT attenuation of 100% brine saturated core, H.U.
Y_{gm} = CT attenuation dry core, H.U.
Y_{brine} = CT attenuation of brine, H.U. (constant)
Y_{gas} = CT attenuation of air, H.U. (constant)

Single Energy Method

$$S_o = (Y_{bgom} - Y_{bm}) / (\phi (Y_{brine} - Y_{oil})) \quad (2)$$

$$S_b = 1 - S_o \quad (3)$$

where:

S_o = Oil saturation
S_b = Brine saturation
Y_{bgom} = CT attenuation of fluid saturated core, H.U.
Y_{oil} = CT attenuation of oil, H.U. (constant)

Dual Energy Method

For each voxel of the sample one can write the following equations, which are an extension of the single energy case to the dual energy and describe the X-ray attenuation due to the combined effect of oil, brine, gas and rock matrix:

$$(Y_{b1} S_b + Y_{g1} S_g + Y_{o1} S_o) \phi + Y_{m1} (1 - \phi) = Y_{bgom1} \quad (4)$$

$$(Y_{b2} S_b + Y_{g2} S_g + Y_{o2} S_o) \phi + Y_{m2} (1 - \phi) = Y_{bgom2} \quad 5)$$

$$Y_{g1} \phi + Y_{m1} (1 - \phi) = Y_{gm1} \quad (6)$$

$$Y_{g2} \phi + Y_{m2} (1 - \phi) = Y_{gm2} \quad (7)$$

$$S_b + S_o + S_g = 1 \quad (8)$$

First, Y_{m1} is eliminated between Eqs. 4 and 6 and Y_{m2} between Eqs. 5 and 7, respectively. This will yield three equations with the unknowns S_b, S_o, and S_g. This system is solved to yield the following expressions for saturations:

$$S_o = A / B \quad (9)$$

$$S_b = C / B \quad (10)$$

$$S_g = 1 - (S_b + S_o) \quad (11)$$

where:

$$A = (Y_{b1} - Y_{g1}) (Y_{bgom2} - Y_{gm2}) - (Y_{b2} - Y_{g2}) (Y_{bgom1} - Y_{gm1}) \quad (12)$$

$$B = \phi [(Y_{b1} - Y_{g1}) (Y_{o2} - Y_{g2}) - (Y_{b2} - Y_{g2}) (Y_{o1} - Y_{g1})] \quad (13)$$

$$C = (Y_{bgom1} - Y_{gm1}) (Y_{o2} - Y_{g2}) - (Y_{bgom2} - Y_{gm2}) (Y_{o1} - Y_{g1}) \quad (14)$$

S_g = Gas saturation
Y_{bgom1} = CT attenuation of fluid saturated core at 125 kV, H.U.
Y_{bgom2} = CT attenuation of fluid saturated core at 96 kV, H.U.
Y_{m1} = CT attenuation of core matrix at 125 kV, H.U.
Y_{m2} = CT attenuation of core matrix at 96 kV, H.U.
Y_{gm1} = CT attenuation of gas saturated core at 125 kV, H.U.
Y_{gm2} = CT attenuation of gas saturated core at 96 kV, H.U.
Y_{b1} = CT attenuation of brine at 125 kV, H.U.
Y_{b2} = CT attenuation of brine at 96 kV, H.U.
Y_{o1} = CT attenuation of oil at 125 kV, H.U.
Y_{o2} = CT attenuation of oil at 96 kV, H.U.
Y_{g1} = CT attenuation of air at 125 kV, H.U.
Y_{g2} = CT attenuation of air at 96 kV, H.U.

Initial experiments concentrated on establishing accurate porosity and two-phase (brine/oil) dual energy saturation measurements as compared with volumetric data. The dual

energy equations were validated by comparing single and dual energy saturations at two-phase saturation conditions. After establishing accurate porosity and two-phase results, a third phase (gas) was introduced into the rock, and three-phase saturations determined by the dual-energy method were compared to volumetric data.

Experimental Results

A Berea core 7.6 cm long and 5.08 cm diameter was outfitted with flow distribution endpieces and jacketed in epoxy. The dry core was placed on the CT table, and cross-sectional slices were taken along the flow direction of the core using 125 kV and 96 kV energies at 8-mm intervals with an 8-mm slice thickness. The oil and brine attenuation numbers were determined by CT scanning a Berea core sample with the respective fluid placed in a five spot pattern of 1/4-in. tubes located within holes drilled in the sample. The fluid characteristics and attenuation values are shown in Table 1. The sample was then saturated under vacuum with an 8% NaI brine, and a volumetric porosity of 22.9% was calculated. The sample was CT scanned at 100% brine saturation using both energies. The average porosities calculated for 125 kV and 96 kV were 22.3 and 22.2%, respectively, within the CT experimental uncertainty and in close agreement with the 22.9% porosity determined volumetrically.

Two-phase endpoint brine/oil saturations were established followed by several three-phase saturation conditions. Table 2 shows the comparison of the average saturation values obtained from volumetric, single energy, and dual energy calculations for 3 two-phase conditions and 3 three-phase conditions. In floods 1 through 3, two-phase saturation conditions were established by (1) injecting 1 pore volume (PV) of oil, (2) injecting 10 PV of oil to attain irreducible brine saturation, and (3) flooding the core to irreducible oil by injecting 10 PV of brine. In floods 4 through 6, three-phase saturation conditions were established by (4) injecting 1,000 PV of gas to establish irreducible brine and oil saturations, (5) displacing the brine with 10 PV of oil to an irreducible brine and gas condition, and (6) injecting an additional 10 PV of oil in the reverse direction. Agreement between the CT and volumetric gas saturations was obtained for all six floods. Close agreement was observed for the CT and volumetric brine and oil saturations for floods 2, 3, and 4, in which a uniform saturation distribution was established. Discrepancies between the CT-derived brine and oil saturations and the volumetric values were observed in floods 1, 5 and 6. In all these cases, nonuniform fluid saturation distributions were observed. Figure 11 shows two saturation profiles (longitudinal and transversal) of the core after the completion of flood 5. The nonuniform gas saturation present in the core is easily noticed, the lighter areas representing zones with higher gas saturations. Figure 12 similarly shows the saturation profiles after reversing the flow direction (flood 6). This resulted in a more uniform distribution of fluids in the core and a better agreement between the CT determined brine and oil saturations and the volumetric values. The discrepancy between the CT and volumetric saturations in a nonuniform fluid distribution case is caused by the use of a constant value for the brine and oil fluid attenuation numbers in the dual energy equations. To improve the saturation values, three dimensional arrays of fluid attenuation values for both phases had to be used for the particular rock system studied. A method is being developed to generate the fluid attenuation arrays and to optimize the CT attenuation contrast between brine and oil.

NUCLEAR MAGNETIC RESONANCE IMAGING MICROSCOPY

To understand the behavior of reservoir and EOR fluids in a core and to improve the EOR processes, direct observation of fluids in the pores of reservoir rock is desired. Nuclear magnetic resonance imaging (NMRI) microscopy is a powerful technique which can provide 3-D images of the fluids in pores.

Equipment Development

To achieve spatial resolutions in the 20 micron range, a new gradient coil assembly, which produces imaging gradients approximately seven times stronger than those previously attained, was designed and constructed this year. The X-, Y-, and Z-gradient coils were wound on separate coil forms and then shaped and mounted in position on fiberglass forms. After completing each layer and connecting the separate coils in series, the coils were imbedded in the fiberglass resin. This created a strong and stable structure for the assembly. The gradient assembly was designed to fit over the standard NMR sample probes as well as the new sample probe described below. Preliminary tests of the gradient coil assembly showed that each of the X-, Y-, Z-gradient coils produced a gradient strength of approximately 1,700 milliTesla/meter, an increase by a factor of seven compared to the previous gradient coils. At this gradient strength, imaging an object 1 cm across using the proton frequency of the NMR spectrometer of 270 MHz would require a data acquisition bandwidth of 724,000 Hz, about seven times larger than the current NMR spectrometer bandwidth, which is only 100,000 Hz. The much stronger gradient fields produced by this coil system will permit the imaging of fluids in sandstones at resolutions below 20 microns.

A new NMRI imaging probe was designed and constructed this year. The radio-frequency (RF) coils are more efficient and can generate the shorter 90-degree RF pulses required for projection reconstruction NMRI at the higher gradients which can be attained with the new gradient assembly described above. The new probe design utilizes a horizontal sample orientation with solenoidal RF coils rather than the current vertical saddle-coil arrangement found in the standard probes. The probe circuit displays a high Q factor (110) and a suitable tuning range which covers both the proton and the fluorine frequencies of 270.2

MHz and 254.2 MHz, respectively. Changing samples requires the probe assembly to be removed from the NMR magnet to gain access to the sample. However, because completing an imaging experiment requires several hours for each sample, this process will not significantly extend experimental time. The new probe also eliminates the interference from proton-containing materials, used in the construction of the standard NMR probes, which create artifacts in the proton NMRI images. These artifacts are particularly serious in the data acquired in the strong gradient fields used for high-resolution NMRI of fluids in porous rock. Preliminary tests of the probe with a water sample showed that the proton 90 degree pulse length was 8.4 microseconds which is four times more efficient than the pulses generated by the standard probes. For comparison, the JEOL 5-mm and 10-mm sample probes have pulse lengths of 16 and 23 microseconds, respectively. The shorter pulse length is needed for high resolution imaging with the stronger gradient fields generated by the new gradient coil system.

Data acquisition has been improved to achieve the higher data acquisition bandwidth required by the addition of a high-speed, two-channel A/D board and a 25 MHz 386 computer. The A/D board can simultaneously sample the two phases of the quadrature NMRI signal at up to 1 MHz rate and store them in the computer memory, bypassing the data file transfer from the NMR spectrometer to the 25 MHz 386 computer for processing. The higher conversion rate of 1 MHz is 10 times that of the built-in A/D converter in the NMR spectrometer. This permits digitizing the higher bandwidth signals (724 kHz for a 1-cm sample) resulting from the stronger gradients achieved with the new gradient system. Also, the capability of direct data acquisition of the 386 computer saves considerable time for the large image files. A set of software drivers for operating the A/D board was obtained, and software for translating the data file format to NMR standard data format was written and tested. These programs use the drivers for the high-speed A/D board to acquire NMR data from the spectrometer, sum the data for multiple scans, and write the data to a file on the 386 computer. Use of the A/D board with these drivers eliminated the time-consuming step of transferring the data files from the NMR spectrometer to the 386 computer where the data processing is performed and images are generated. Figure 13 shows, in schematic form, the operation of the NMRI system incorporating the different components previously discussed. The NMR spectrometer block represents the standard instrument with the RF components which transmit and detect the NMR signals and the pulse programmer which controls the timing of the signal acquisition process. The 25 MHz 386 PC block represents the added high-speed data acquisition capability and the imaging gradient switching and amplitude control. Also shown in Fig. 13 are the gradient amplifiers, the gradient coil system, and the sample probe. The probe contains the RF coils which surround the sample and transmit the NMR frequencies to the sample and receive the image signals. Control software, running on a 25 MHz 386 PC, monitors the gradient timing gate and receiver gate signals from the spectrometer pulse programmer. Upon receipt of the gradient gate signal the PC outputs the appropriate gradient signal through the digital/analog (D/A) board. Upon receipt of the receiver gate signal the high-speed two-channel A/D system starts acquiring the image signals and writes them to a data file on the PC disk drive. Advantages of the above approach in spectrometer modifications are the expanded NMRI signal bandwidth capabilities of the high-speed A/D system reconstruction software. Also shown is the 33 MHz 386 computer with a Weitek coprocessor which now is used exclusively to process the data transferred to it from the 25 MHz 386 computer. This permits data to be acquired on the 25 MHz 386 PC for one experiment while an earlier data set is being processed on the 33 MHz 386 PC. The capability reduces the turnaround time (acquisition plus processing) by half, which for 256 x 256 x 256 images can mean a time reduction from 48 to 24 hr. The data files are transferred between the two 386 computers using Brooklyn Bridge software through the parallel printer ports. This permits transfer of the large image data files to the processing computer in only a few minutes. A Syquest removeable cartridge drive was obtained for the processing computer. Several image files can be stored on one cartridge instead of many floppies. The DOS Syquest cartridges then are read by the Mac IIfx workstation on which the image display and analysis is performed.

NMRI Measurements and Results

A new sample cell was made for the horizontal solenoid NMRI sample probe. The sample cell has a sample cavity 3 mm in diameter and 6 mm long. The sample cell is made of Teflon with nylon endcaps which seal against the inlet and outlet tubes with O-rings to form a positive seal. Using polymer beads having a size range of 250 to 350 microns, a beadpack was made in the sample cell and saturated under vacuum with water. NMRI images of the bead pack have been obtained at 128 x 128 x 128 pixels and 256 x 256 x 256 pixels. The pixel size at the lower resolution is 30 microns while at the higher resolution a pixel size of 15 microns was obtained which is the highest spatial resolution achieved to date by this laboratory. Figure 14 shows an MRI image of the beadpack at the higher resolution. The circular silhouettes of the beads can clearly be seen. Water, which occupies the voids between the beads, appears as the brighter area. This image was achieved by using the new horizontal probe and the strong-gradient coil assembly recently constructed. The image acquisition time was 17 hr and the data processing of the 32 megabyte raw data file lasted 25 hr on the 33 MHz 386 computer. If such measurements are to be performed routinely, then a RISC-based workstation would reduce the data processing time to provide a total turnaround time for the experiment of less than 24 hr. The new workstation also has been used to display a 3-D NMRI data set from a sandpack. Previous image analysis software was restricted to a 2-D display of cross sections through the sample. This workstation permits the 3-D display of the structure of the fluid contained in the pore network of the sample.

Software was written to reformat the NMRI data set to the format required for the workstation. Figure 15 shows the pore network structure for a sandpack containing oil as the saturating fluid. The cubical section shown is a small part of the total sample image located near the top edge of the sample. The dimensions of the block are 1.8 mm per side. The sand grains used to make the pack had diameters from 350 to 500 microns. The shades of gray represent the pore spaces, while the grains component of the sample have been rendered transparent to show the interior structure of the pore network. Details of the pore network in the 50 micron range are clearly visible. Using the new probe and gradient coil, NMRI images of fluids in a native sandstone rock sample at high resolution have been obtained. The sample was a small plug of water-wet Bentheim sandstone 4 mm in diameter and 7 mm long. A Teflon coreholder was made which fit snugly around the rock plug. Nylon endcaps, with O-ring seals which fit tightly around smallbore Teflon tubing (0.0625 in. OD) and used as inlet and outlet ports, permitted the exchange of fluid while the sample was inside the imaging probe inside the NMR magnet. The Bentheim plug was initially saturated with water under vacuum. The water contained 0.003M $MnCl_2$ as a relaxation agent. Longitudinal relaxation time (T1) measurements showed the aqueous phase had a T1 time of 47 milliseconds. Several images of the aqueous phase were made at pixel resolutions of 128 x 128 x 128 and 256 x 256 x 256. A gradient strength of 75 Gauss/cm was used. At the highest resolution the pixel size was 25 microns in the cross-sectional views with 40 microns along the axis. These are the highest resolution images reported to date of fluids in sandstone. Soltrol mineral oil, with the viscosity adjusted to 5 cP, was injected into the water-saturated Bentheim plug (2 mL or about 100 PV was used). The injection was done under gravity flow with a fluid head of about 8 ft. The T1 measurement of the oil phase gave a T1 value of 523 milliseconds. Two images of the plug were made at a pixel resolution of 256 x 256 x 256, one showing the oil distribution (Fig. 16), and the second showing the residual water phase using an inversion recovery imaging sequence to null the oil phase signal (Fig. 17). Notice that the water appears as small isolated droplets filling the small pores while the oil phase fills the large pores. Because of the longer T1 value for the oil and the lower signal/noise ratio for the residual water, each of these images took approximately 75 hr to acquire.

THIN-SLAB MICROMODEL MICROSCOPY

A videotape, which contains sample images (both monochromatic and color) of fluids in the pores of Berea and Bentheimer rocks,[5] has been prepared from the micromodel fluid-flow experiments performed in FY90. The video is provided as a technology transfer device in place of photographs because of the high velocity events and the difficulties and cost involved in the mass reproduction of numerous high quality photographs required in depicting complex dynamic behavior. This document gives a proper perspective of this innovative technique and its potential for microscopic study of rock/fluid dynamics.

Experimental Technique

A 2-to 3-mm thick, 25-mm diameter slab is cut from a core and encapsulated between two transparent plates. The metalic frame that holds this rock/glass assembly is drilled to provide ports for fluid injection and production in and out of the rock slab. The glass surfaces are pre-coated with transparent silicon rubber to ensure that a good seal is formed with the rock surfaces upon assembly. The fluids are confined to the rock by rubber gaskets and silicon rubber seal. The assembled rock-slab micromodel is then mounted on a standard transmitted-light microscope with imaging capabilities. Fluids are injected using syringe pumps and the micromodel is scanned and imaged during and after injection.

Scope and Limitations

The images in the video were selected to show the potential of this technique. These images were processed using standard off-the-shelf consumer video products: a camcorder and a VCR, both of super-VHS format. The only speciality component was a VHS format video processor, with signal improvement (enhancement/noise reduction), color control (tint, intensity, brightness, black pedestal, and white level), and chroma/lumin invert capabilities. The video processer was instrumental in transforming the marginal images to a useable form, but because of its VHS format, was a costly trade-off in resolution. The quality of the images can be substantially improved with top-of-the-line commercial video equipment, such as a three-chip RGB camera, a 3/4 in. or larger tape-size video deck with advanced editing capabilities, and a super-VHS advanced video processor. The image quality can also be improved by using more appropriate microscope objectives, a brighter light source, and contrast enhancement accessories.

Whereas the image quality can be substantially improved, questions concerning scaling differences remain unanswered for rock-slab or any other micromodel. The influence of the enclosing plates of non-matching wettability has to be carefully deciphered in the planning and analysis of experiments. The so-called end effects, because of capillary discontinuity at the external boundaries, have the potential to mask the true behavior. Choosing experimental conditions to minimize such problems is an essential component in carrying out micromodel experiments.

Even though not always guaranteeing realistic behavior, the rock-slab micromodels are closer than any other technique. There are many instances, especially those not dominated by viscous forces, in which rock-slab models can provide information not otherwise possible.

Observations

The following are practical observations regarding thin-slab micromodel investigations:

1. Monochromatic images, even though offering higher resolution under low light conditions, are not effective in discerning complex, multiphase fluids in porous media. Color images are successful in imaging multiple fluids in porous media.

2. During secondary drainage (oil reinjection), water encroachment caused oil to flow in the form of discrete bubbles.

3. Turbulence at the microscopic level was frequently observed at injection rates corresponding to 1 to 10 ft/d nominal front velocity. Spinning of the oil bubbles along their own major axis was observed.

4. Oil transport, at least in part, was in the form of a snap-off/coalesce sequence at lower rates when capillarity forces dominated the flow.

5. At the start of oil injection, the bubbles were several-fold smaller than the pores. As the oil throughput increased, some of these bubbles coalesced and consequently were trapped due to the restrictive pore morphology.

6. Because of this noncontinuous advancement of oil (non-wetting fluid), the pressure field was also fluctuating. Large bubbles were seen advancing and retracting at a fixed general location.

7. Surfactants were effective in generating foam in situ even in the presence of residual oil. Foam that was not held stationary, flowed in small bubbles.

8. Flow in the form of an emulsion was also observed.

RESULTS AND CONCLUSIONS

- Permeability-porosity correlations obtained from image analysis were combined with porosity distributions from CT scanning to generate spatial permeability distributions within core.

- Simulation-derived saturation distributions of two-phase processes showed very good agreement with the CT-measured values.

- The addition of a computer controlled high accuracy positioning table and direct interfacing of the CT scanner to a workstation for 3-D image analysis has considerably increased the efficiency, accuracy, and versatility of the CT laboratory.

- Improvments were made in the measurement of gas saturations by CT scanning, and progress has been made toward accurate measurement of three-phase fluid saturations.

- Newly constructed gradient coils and probe and improved data acquisition and processing greatly enhanced the spatial-resolution measurement of fluids in porous media by NMRI microscopy.

- Use of the imaging facility in support of DOE-funded Base Research programs and industrially-sponsored projects was expanded.

- A videotape highlighting potential applications of the thin-slab micromodel technology for the pore level study of fluids has been produced as an instrument for technology transfer.

To expand the impact which the rock-fluid imaging technology developed at NIPER has on understanding fundamental oil recovery phenomena and in helping the oil industry in solving practical problems, the following objectives are planned for the next fiscal year: (1) To develop a methodology to derive reservoir engineering parameters from petrographic, computed tomography (CT) scanning, and nuclear magnetic resonance (NMRI) images. (2) To characterize the recovery efficiency and to measure the saturation distributions in cores for EOR processes applicable to specific reservoirs, including Class I, by using the developed state-of-the-art imaging technology. (3) To investigate the applicability of imaging technologies to the development of scale-up procedures from core plug to whole core to interwell scale. (4) To develop an industry consortium or industrial advisory panel organized to help plan, review, and participate in the research through the Work-For-Others category of the IITRI/DOE Cooperative Agreement and to provide for effective technology transfer. (5) To strongly encourage and seek cost-sharing of collaborative research by industrial participants.

ACKNOWLEDGMENTS

The authors wish to acknowledge the constructive input from Drs. Tom Burchfield and Michael Madden of NIPER; the support of Alex Crawley and Bob Lemmon of the Bartlesville Project Office of the U.S. Department of Energy; and the financial support of the U.S. Department of Energy through Cooperative Agreement DE-FC22-83FE60149.

REFERENCES

1. Tomutsa, L. *Application of Imaging Techniques to Other Field and Laboratory Projects*. DOE Report NIPER-572, September 1991.
2. U. S. Department of Energy. *National Energy Strategy*, First Edition 1001/1002, Washington, DC, February 1991, p 78.
3. Tomutsa, L., D. Doughty, S. Mahmood, A. Brinkmeyer and M. Madden. *Imaging Techniques Applied to the Study of Fluids in Porous Media*. DOE Report NIPER-485, January 1991.
4. Tomutsa, L., and A. Brinkmeyer. *Using Image Analysis To Determine Petrophysical Properties of Reservoir Rocks*. DOE Report NIPER-444, 1989.
5. Mahmood, S. M., D. Doughty, L. Tomutsa, and M. Honarpour. *Pore Level Fluid Imaging Using High Resolution Nuclear Magnetic Resonance Imaging in Thin Slab Micromodels*. Pres. at the 1990 Ann. Technical Conf. of the Society of Core Analysts, Aug. 13-15, 1990, Dallas, TX. SCA paper 9024.

TABLE 1. Fluids and attenuation values at two X-ray energies

Fluid	X-Ray Energy 125 kV	96 kV
Air	-499	-500
8 wt % NaI Brine	562	803
47.5 wt % Bromodecane in Soltrol-100	254	391

TABLE 2. Comparison of three-phase fluid saturaton computations: volumetric, dual energy, and single energy

Flood number and description	Brine Saturation		Single Energy	
	Volumetric	Dual Energy	125 kV	96 kV
1. Oil flood 1 PV	0.481	0.544	0.416	0.437
2. Oil flood 10 PV	0.385	0.375	0.378	0.385
3. Brine flood 10 PV	0.725	0.721	0.696	0.704
4. Gas flood 1,000 PV	0.402	0.469		

Flood number and description	Oil Saturation		Single Energy	
	Volumetric	Dual Energy	125 kV	96 kV
1. Oil flood 1 PV	0.519	0.386	0.584	0.563
2. Oil flood 10 PV	0.615	0.623	0.623	0.615
3. Brine flood 10 PV	0.275	0.270	0.301	0.296
4. Gas flood 1,000 PV	0.264	0.179		

Flood number and description	Gas Saturation		Single Energy	
	Volumetric	Dual Energy	125 kV	96 kV
1. Oil flood 1 PV	0.000	0.071	N/A	N/A
2. Oil flood 10 PV	0.000	0.003	N/A	N/A
3. Brine flood 10 PV	0.000	0.009	N/A	N/A
4. Gas flood 1,000 PV	0.334	0.353		
5. Oil flood 10 PV	0.116	0.158		
6. Oil flood 20 PV	0.105	0.099		

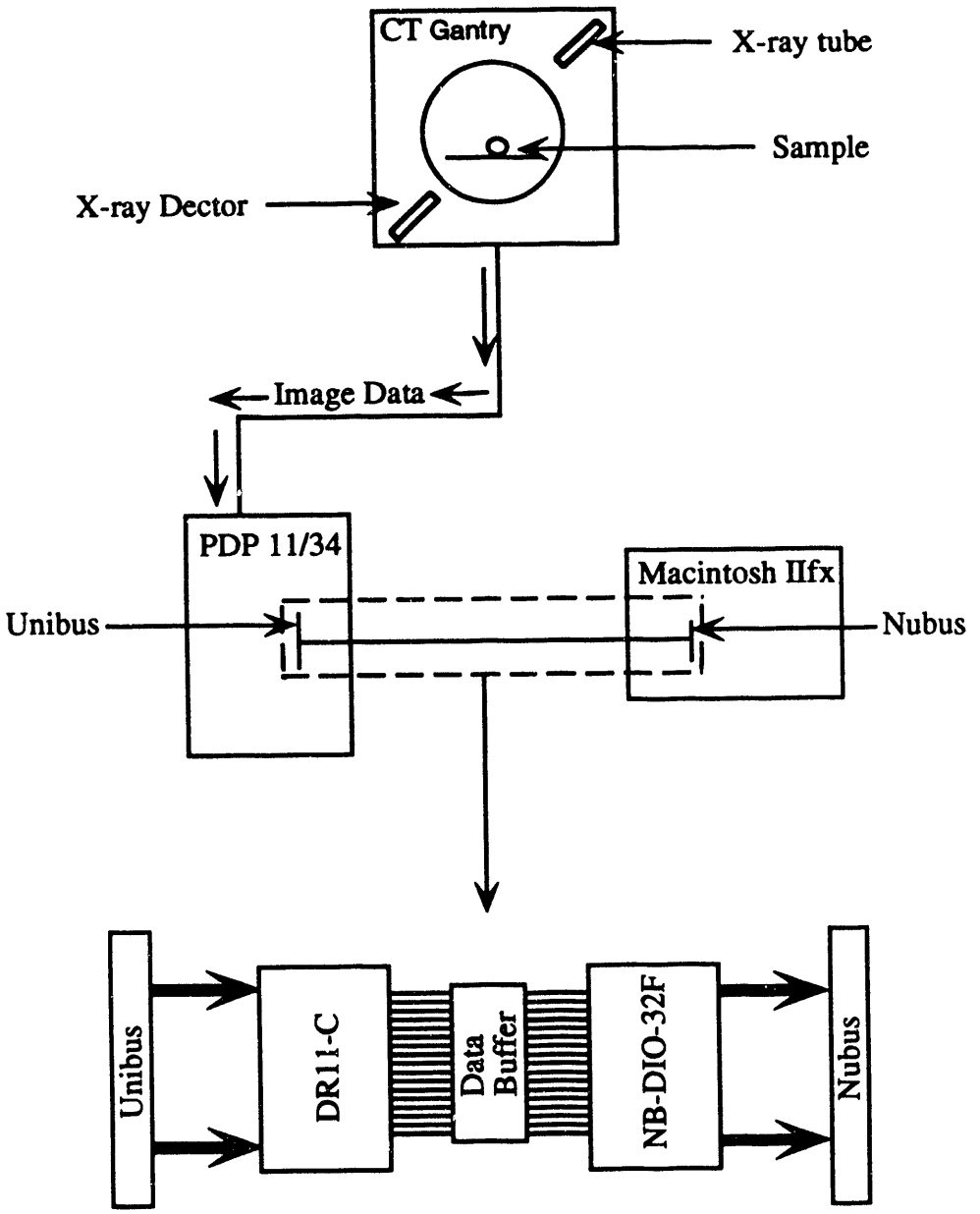

FIGURE 1. - Schematic diagram of CT image capture system.

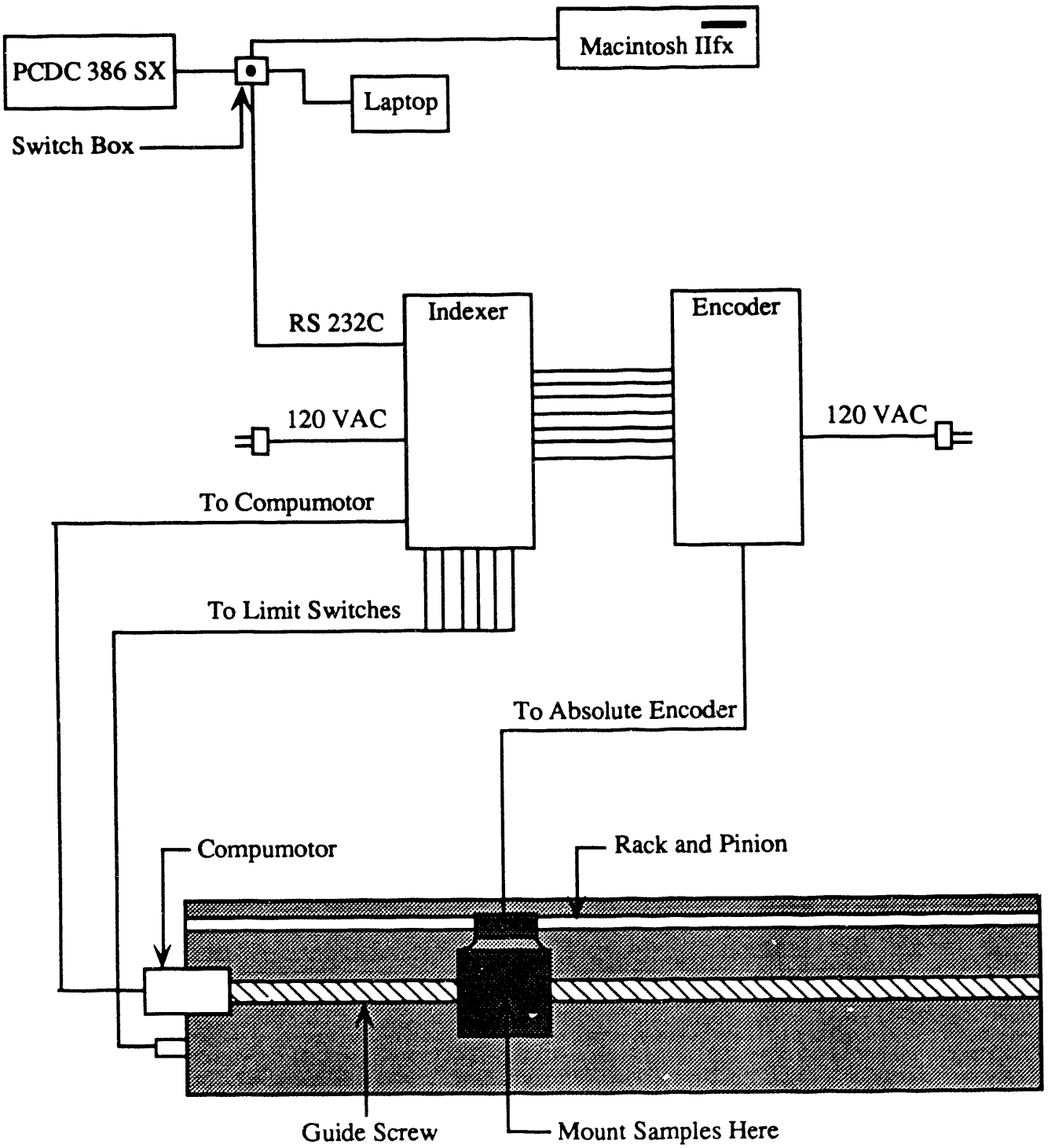

FIGURE 2. - CT positioning system.

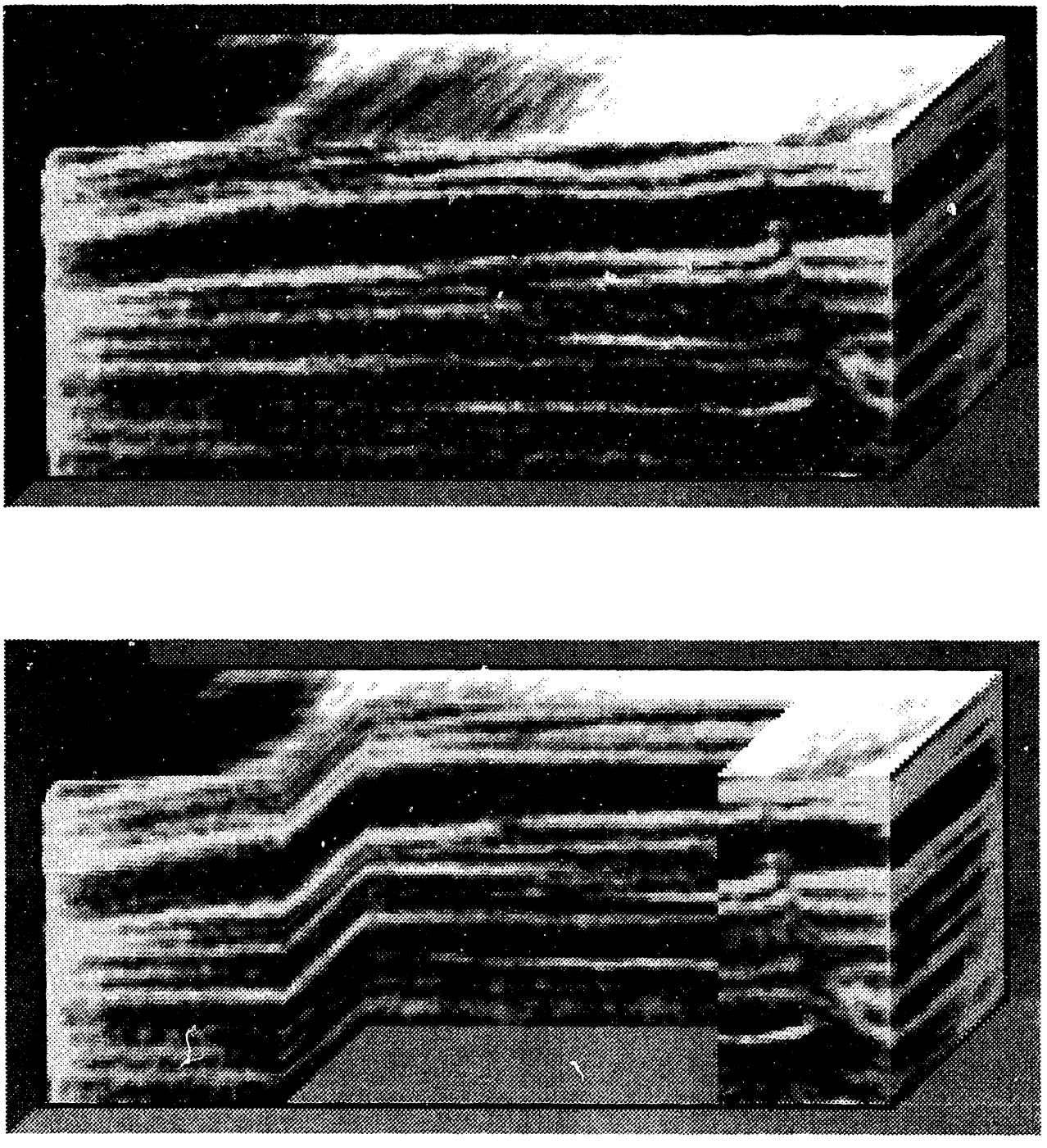

FIGURE 3. - CT image of layered Shannon slab with higher porosity layers selected for enhanced viewing.

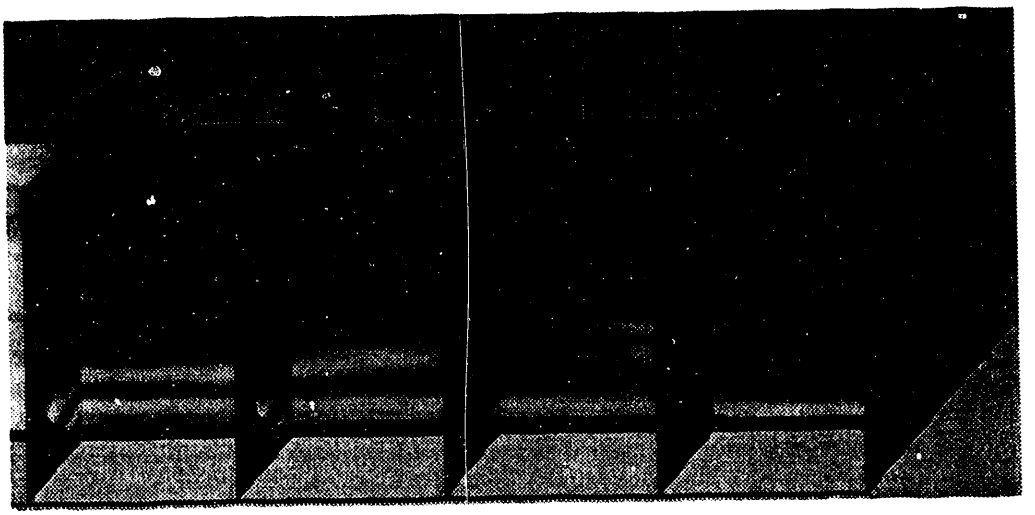

FIGURE 4. - CT image of layered core.

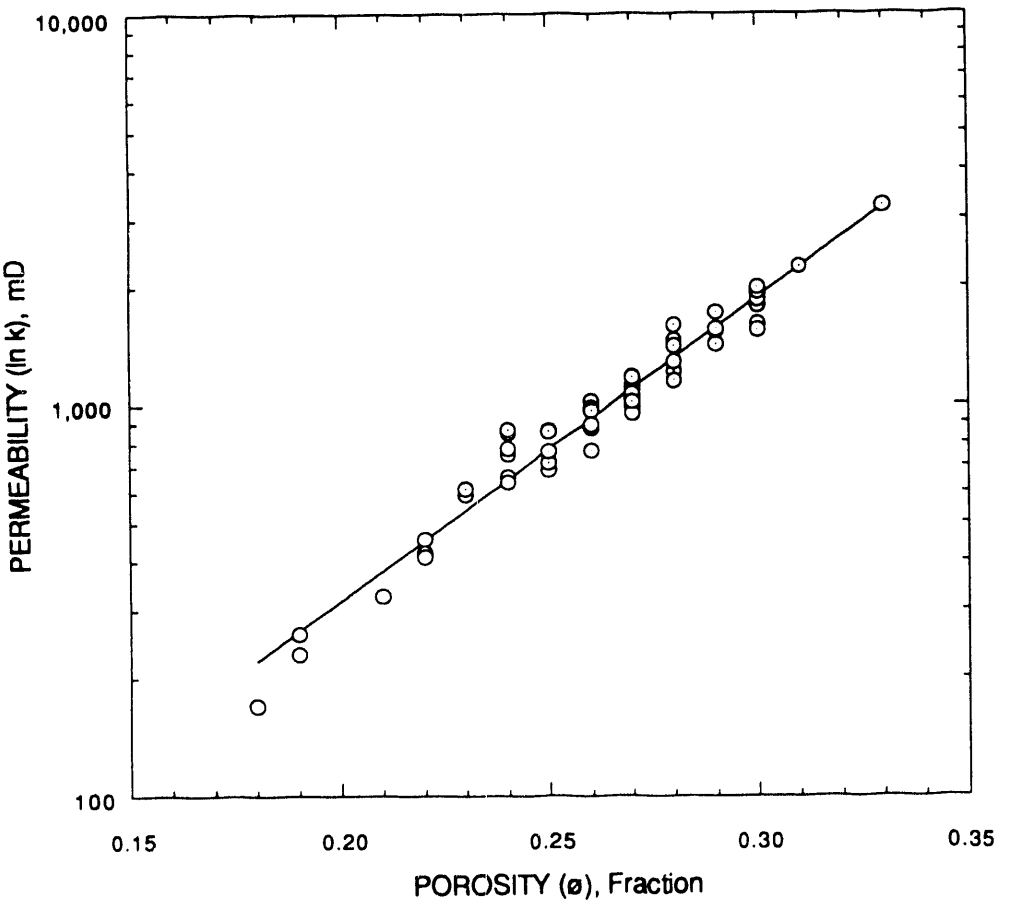

FIGURE 5. - Correlation of permeability and porosity. Data points represent experimental results, whereas the straight line represents the least-squares best fit according to the equation ln (k) = 8.921 + 17.841 ø, r = 0.980.

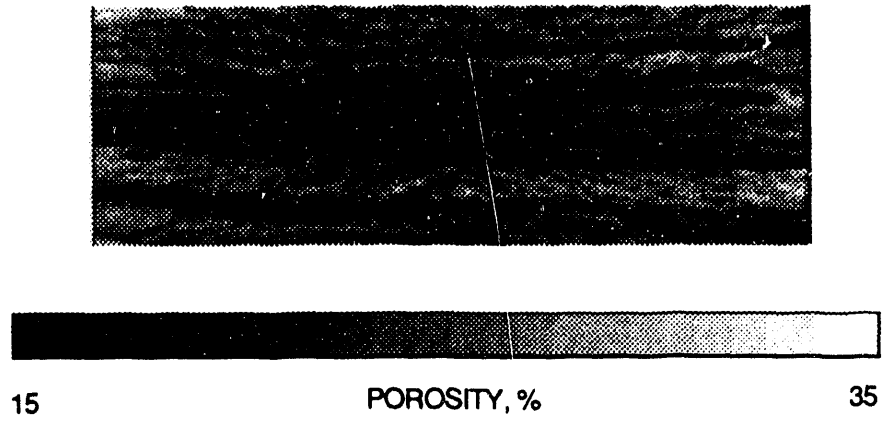

FIGURE 6. - Porosity and permeability distribution from Shannon sandstone slab.

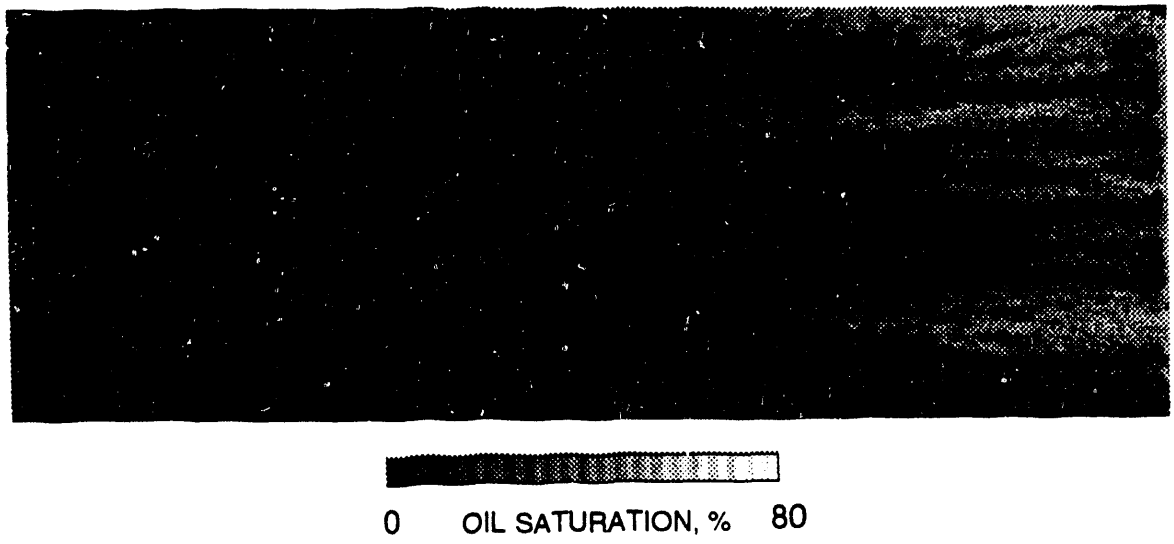

FIGURE 7. - CT scan of oil flood of Shannon sandstone (direction of flow is from right to left).

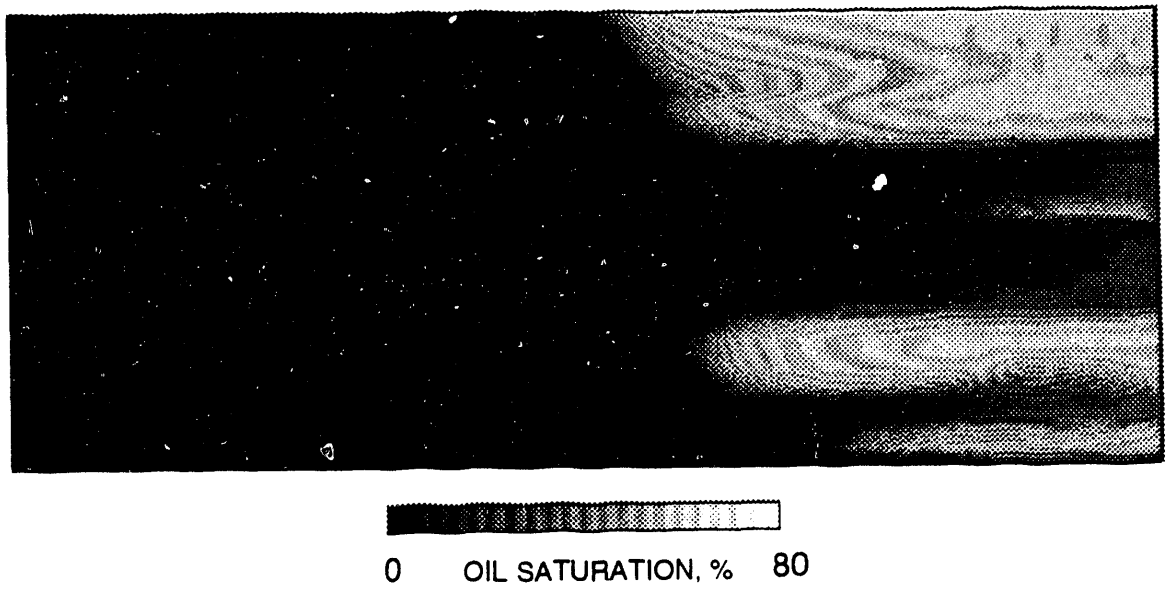

FIGURE 8. - Simulation of oil flood of Shannon sandstone (direction of flow is from right to left).

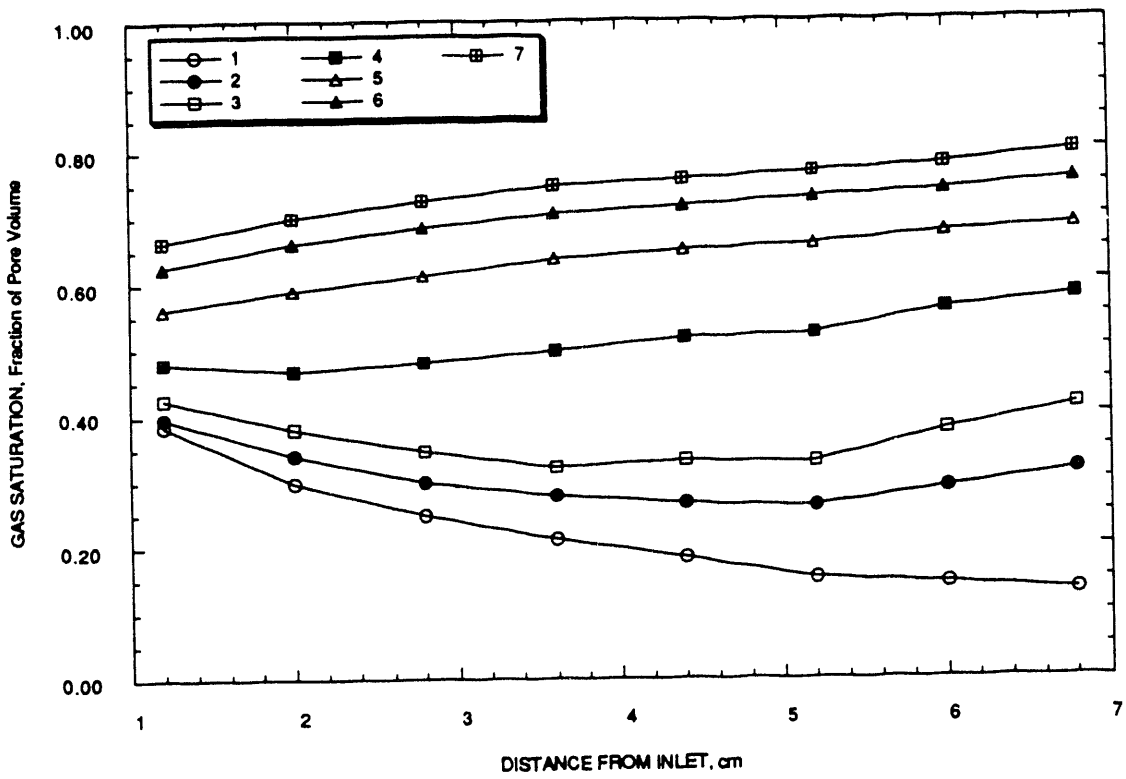

FIGURE 9. - Average cross-section gas saturations for various stages of a gas flood (curves 1 to 7 indicate increasing average gas saturations).

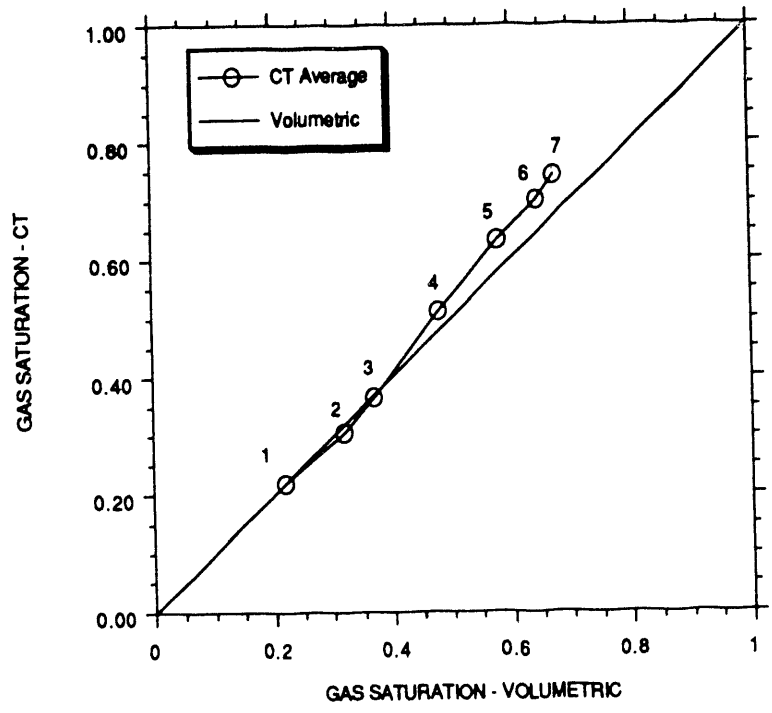

FIGURE 10. - Comparison of CT and volumetric average gas saturations in three-phase flood (numbers refer to saturation curves shown in Figure 9).

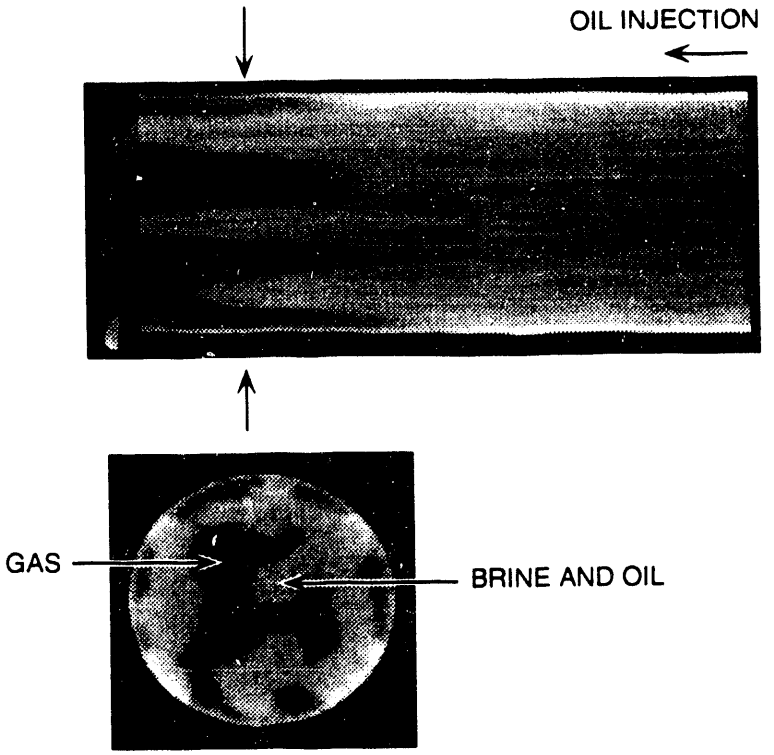

FIGURE 11. - Nonuniform fluid distribution in three-phase flood.

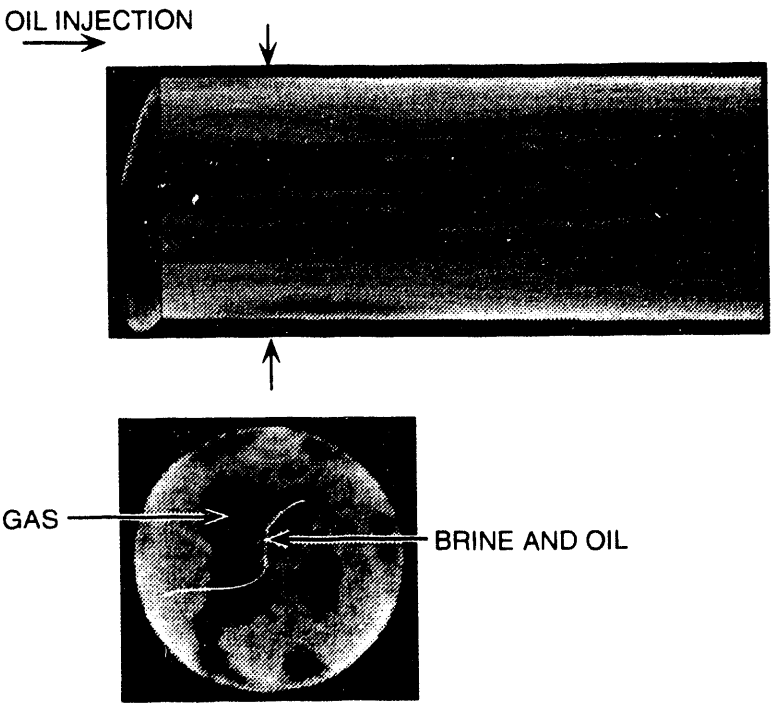

FIGURE 12. - Nonuniform fluid distribution in three-phase flood (reverse flow).

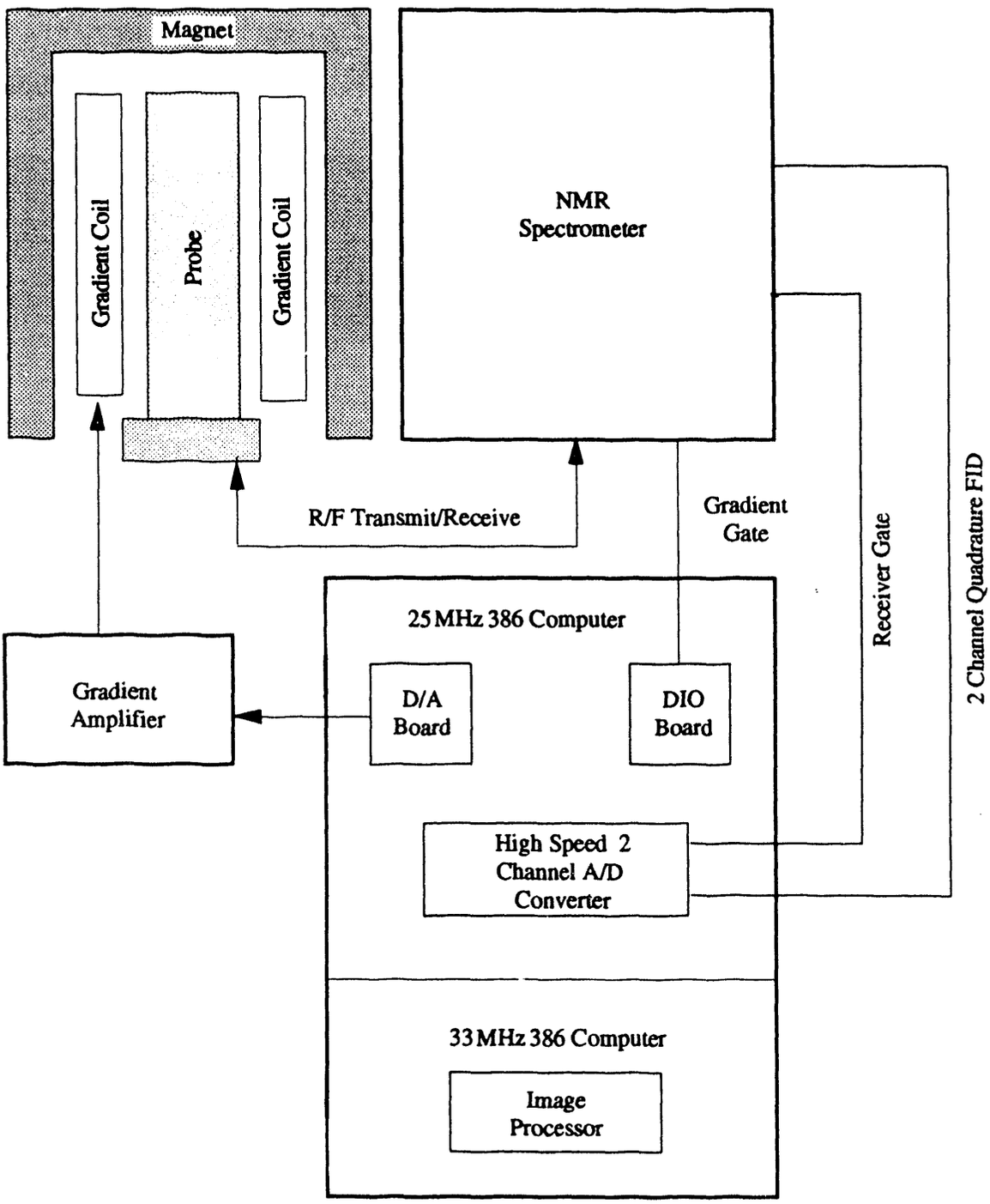

FIGURE 13. - Block diagram of NMRI microscopy system.

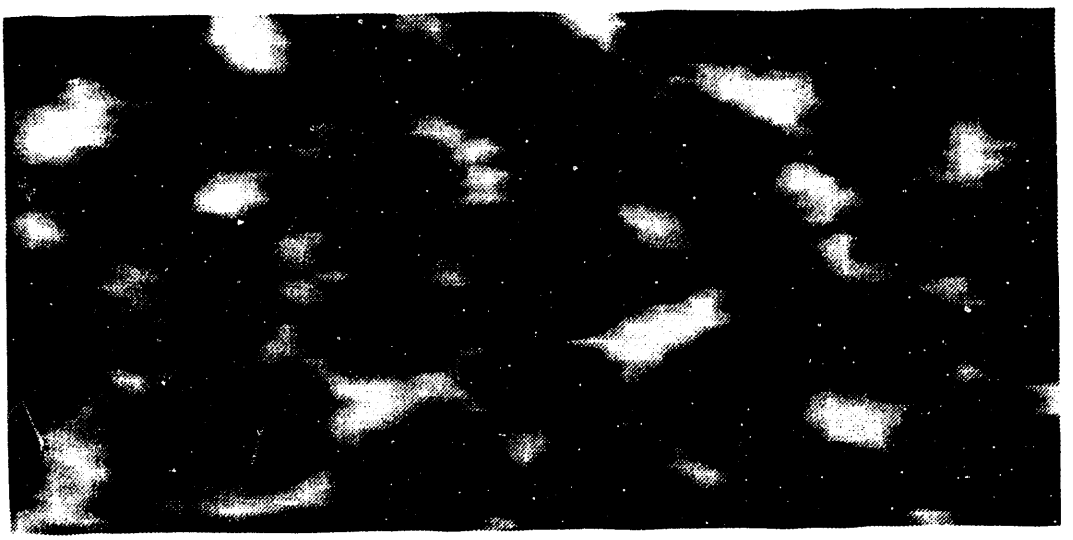

FIGURE 14. - High-resolution NMRI of water saturation in a polymer beadpack (beads are dark, water is light).

FIGURE 15. - NMR image of the oil phase in a sandpack showing an enlarged view of the fluid-filled pores.

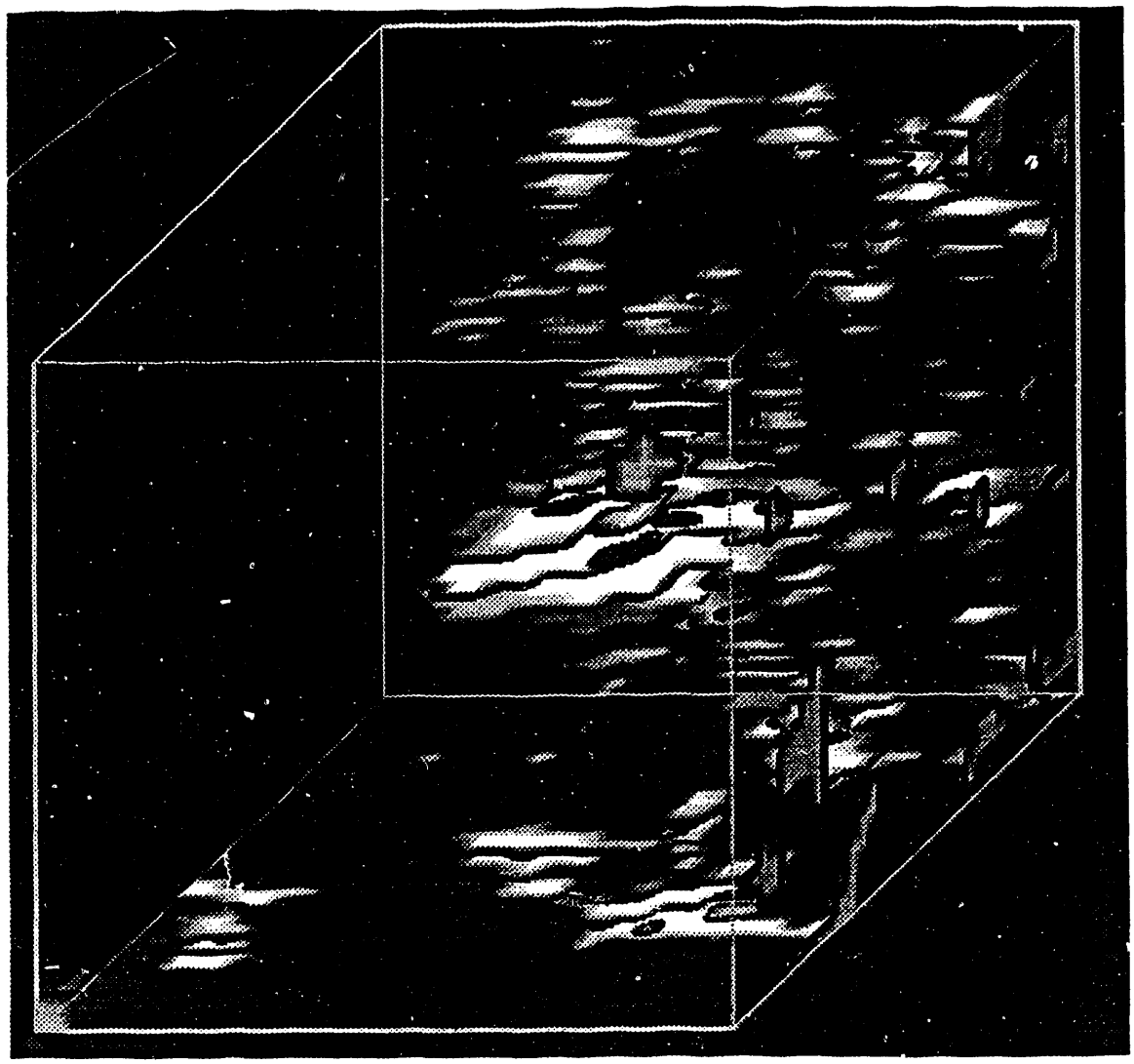

FIGURE 16. - Pore-scale oil distribution at residual water (same block as shown in Fig. 17)

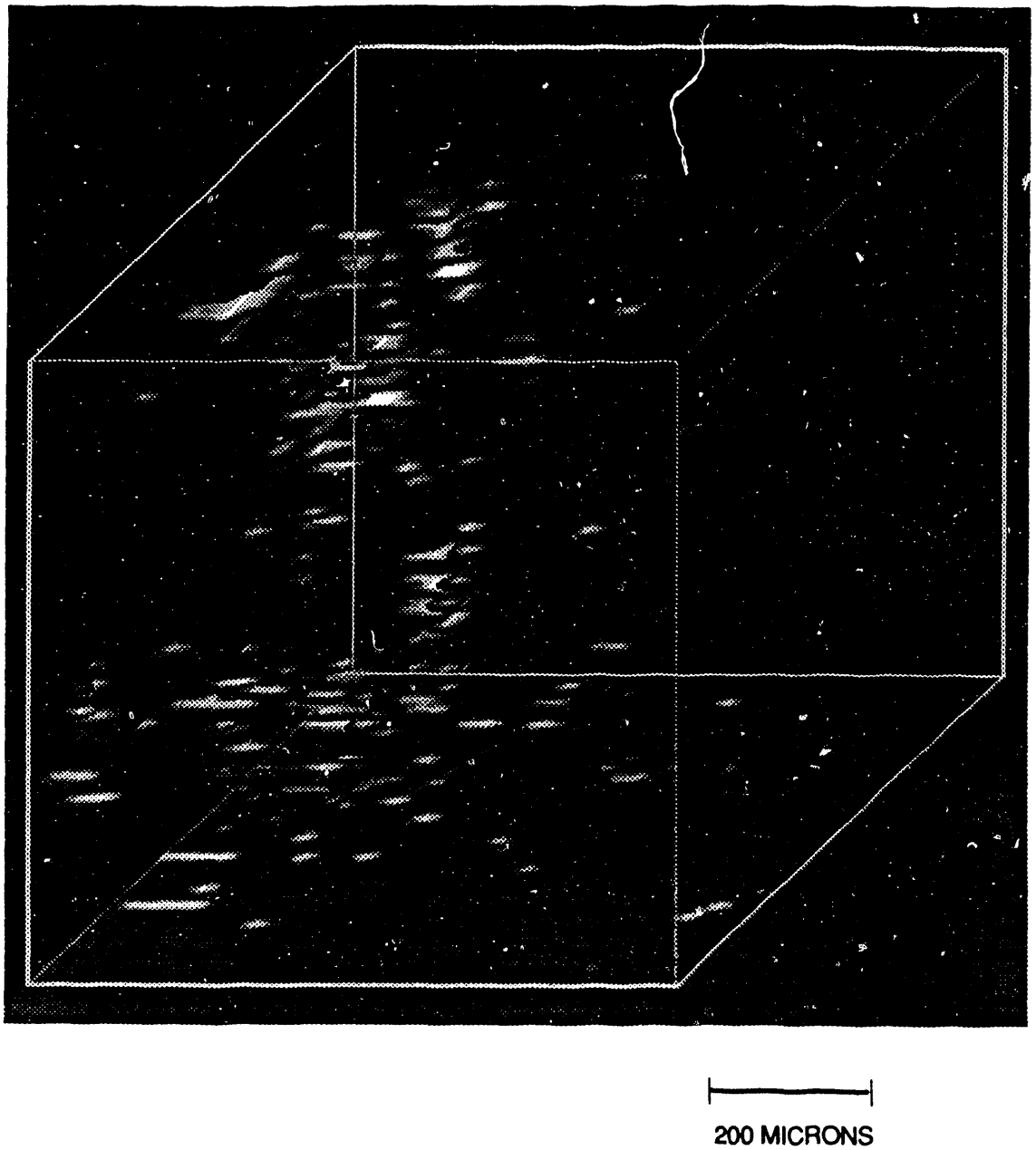

FIGURE 17. - Pore-scale water distribution at residual water (same block as shown in Fig. 16)

*U.S.GPO:1992-661-026/60027